RSC Advances

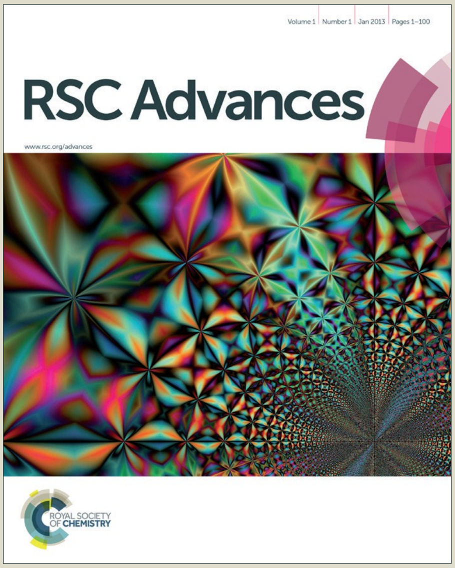

ROYAL SOCIETY OF CHEMISTRY

www.rsc.org/advances

Journal Name

# Ultrafast Electrochemical Preparation of Graphene/CoS Nanosheets Counter Electrodes for Efficient Dye-Sensitized Solar Cells

T088Received 00th January 20xx,
Accepted 00th January 20xx

DOI: 10.1039/x0xx00000x

www.rsc.org/

Chongyang Zhu,[‡a] Huihua Min,[‡a] Feng Xu,*[ab] Jing Chen,[c] Hui Dong,[a] Ling Tong,[d] Yimei Zhu,[b] Litao Sun[a]

Utilizing inexpensive, high-efficiency counter electrodes (CEs) to replace the traditional platinum counterparts in dye-sensitized solar cells (DSSCs) is worthwhile. In this paper, we detail how we synchronously prepared composite CEs of CoS nanosheet arrays and reduced graphene oxide (rGO) layers for the first time via a low temperature, ultrafast one-step electrochemical strategy. With this approach, the whole fabrication process of the composite CEs was only a small percentage of the average time (~15 hours) using other methods. The DSSC assembled with the rGO-CoS composite CE achieved an enhanced power conversion efficiency (PCE) of 8.34%, which is dramatically higher than 6.27% of pure CoS CE-based DSSC and even exceeds 7.50% of Pt CE-based DSSC. The outstanding PCE breakthrough is indubitably attributed to the enhancement in electrocatalytic ability of the rGO-CoS composite CE due to the incorporation of highly conducting rGO layers and the GO layers-induced growth of CoS nanosheet arrays with higher density and larger surface area. Therefore, lower charge-transfer resistance and higher exchange current density can be achieved as corroborated by the electrochemical impedance spectra (EIS) and Tafel polarization curves (TPCs). Further experiments also proved that the electrochemical strategy exhibited its universality of fabricating other graphene-enhanced chalcogenide functional composite films.

## Introduction

Dye-sensitized solar cells (DSSCs) have attracted great attention due to their low cost, easy fabrication, and relatively high power conversion efficiency (PCE)[1–3]. As one of the most important components, a platinum-loaded conducting substrate is commonly employed as the counter electrode (CE) due to its superior electrocatalytic activity toward $I^-/I_3^-$ redox couple[4–7]. However, platinum is rare on earth, and hence, very expensive. Considerable effort has been devoted to developing alternatives to Pt, including functional carbon nanomaterials[8–9], conducting polymers[10–11], and transition-metal compounds[12-14]. Among these, cobalt sulfide (CoS) is regarded as one promising candidate with outstanding electrocatalytic activity toward the $I^-/I_3^-$ redox couple. To date, CoS nanostructures, including those with honeycomb-like morphology, acicular nanorod arrays, nanosheet arrays, and nanotube arrays have been applied successfully as the CEs that exhibit different electrocatalytic activities[15–18]. Obviously, the electrocatalytic activities of the CoS CEs greatly depended on their structures and/or morphologies that are susceptible to the strategies used in their preparation. Moreover, although CoS is an active electrocatalytic species, its charge conductivity and mobility are not up to the mark. Hence, much attention has been paid to incorporating materials with high electronic conductivity into CoS CEs along with optimizing their structure and morphology.

Recently, graphene has triggered much interest due to its excellent electronic conductivity, high transparency, and large specific surface area[19]. These properties make it very promising for applications in the CEs[20-22]. In particular, graphene as highly conductive scaffold has been incorporated into the CoS CEs by numerous methods. For instance, Das *et al.*[23] and Bi *et al.*[24] prepared graphene films via a CVD system that were used as the substrate to fabricate CoS nanoparticle/graphene CEs. However, the CVD method required the utilization of high temperature up to 1000 ℃ to prepare graphene film, which restricted its widespread application. Duan *et al.*[25] fabricated graphene-$CoS_2$ composite CEs through a hydrothermal synthesis and achieved a PCE of 6.55%. Further, Hu *et al.*[26] and Miao *et al.*[27] used electrophoretic deposition to fabricate graphene-CoS composite CEs, but the whole process took up about thirty hours. All these methods suffered from the restrictions of requiring high temperatures, toxic chemical agents, and tedious procedures that are time or labor consuming. Thus, the challenge remains of seeking an efficient, facile, and low temperature route to fabricate graphene-CoS CE.

In this study, we demonstrate how we synchronously prepared composite CEs of CoS nanosheet arrays and reduced graphene oxide (rGO) layers for the first time via a low temperature, ultrafast one-step electrochemical strategy. With this approach, the whole fabrication process of the composite CEs was only a small percentage of the average time (~15 hours) using other methods. In

---

[a] SEU-FEI Nano-Pico Center, Key Laboratory of MEMS of Ministry of Education, Southeast University, Nanjing 210096, China. E-mail: fxu@seu.edu.cn; Fax: +86-25-83792939; Tel: +86-25-83792632.

[b] Condensed Matter Physics & Materials Science Department, Brookhaven National Laboratory, Upton, NY 11973, USA.

[c] School of Electronic Science and Engineering, Southeast University, Nanjing 210096, China.

[d] Jiangnan Graphene Research Institute, Changzhou 213149, China.

[‡] These authors contributed equally to this work.

this strategy, the pre-prepared GO layers on ITO substrates provided a large number of active sites for the nucleation and crystal growth of CoS nanosheets. Thus, denser CoS nanosheet arrays with smaller size were formed compared with the products without incorporation of GO layers. This structure would allow more electrons to transport from external circuit to I–/$I_3$– redox couple due to the relatively large surface area, resulting in improved catalytic activity. More importantly, the oxygen-containing groups on original GO layers also were effectively removed under applied negative potential, and the electronically conductive rGO layers were formed. It's demonstrated that the DSSCs assembled with rGO-CoS composite CEs fabricated by the electrochemical strategy exhibited considerably high PCEs compared with the reported ones with rGO-CoS composite CEs.

## Experimental

### Preparation of rGO-CoS composite CE

Graphene oxide (GO) was prepared by chemically exfoliating graphite via the modified Hummer's method[28–29]. Then, solutions of GO ethanol of different concentrations (0.06−0.12 mg/mL) were spray-coated on the pre-cleaned ITO substrates heated at 50℃, so forming GO layers. Afterwards, the GO layers on ITO substrates acted as working electrodes to electrodeposit CoS nanosheets via a three-electrode electrochemical system with a platinum sheet as a counter electrode (We note that the counter electrode is entirely different from the definition of CEs in DSSCs) along with a saturated calomel electrode (SCE) as a reference electrode. Meanwhile, the GO layers with oxygen-containing groups also were effectively reduced under the applied negative potential and thus, the rGO-CoS nanosheets as composite CEs were realized synchronously[17,30]. The whole electrochemical process was carried out in a 40 mL aqueous solution electrolyte containing 5 mM $CoCl_2 \cdot 6H_2O$ and 150 mM $CH_4N_2S$ at 40 °C. The deposition potential was −0.83V versus SCE, and the deposition time was 0.5 h. For comparison, pure CoS nanosheet arrays as the CE were also directly electrodeposited on ITO substrate without GO layers by a similar electrochemical procedure. The standard Pt CE was purchased from Dalian HepatChroma SolarTech Co. Ltd.

### DSSC fabrication and testing

A layer of $TiO_2$ nanocrystal anode film with a thickness of 12 μm and active area of 0.30 $cm^2$ was prepared by the screen-printing technique and subsequently calcined at 450 ℃ for 30 min. The resultant $TiO_2$ photoanodes were sensitized in a 0.3 mM ethanol solution of ruthenium dye N719 at 60°C for 3h. Then, they were assembled with Pt, CoS, and rGO-CoS CEs into DSSCs, respectively. The DSSC electrolyte with 0.1 M LiI, 0.05 M $I_2$, 0.3 M 1,2-dimethyl-3-propylimidazolium iodine, and 0.5 M tert-butylpyridine in 3-methoxypropionitrile was injected into the gap between the photoanode and CE by capillarity action. The current–voltage characteristics of DSSCs were assessed with a Newport solar simulator (300W Xe lamp source), and a Keithley 2400 source meter under 1 sun illumination (AM 1.5G, 100 mW/$cm^2$).

### Characterization

The phase identification and surface morphology of the products were characterized by a powder X-ray diffractometer (XRD, ARL XTRA, Thermo Electron Co., USA) with Cu $K_\alpha$ radiation and a scanning electron microscope (SEM, JSM-7600F, JEOL, Japan). Further structural analyses were carried out by a transmission electron microscope (TEM, ARM200, JEOL, Japan) and the electron diffraction (ED) pattern. Raman spectroscopy was recorded on Renishaw laser Raman spectrometer, using a 488 nm laser source. Fourier-transform infrared (FT-IR) spectra were collected with an FTIR-650 spectrophotometer by the KBr pellet method. Atomic force microscope (AFM) images were acquired using Bruker MultiMode 8 in a "tapping" mode. Cyclic voltammetry (CV) was carried out in a three-electrode system with an anhydrous acetonitrile solution of 0.1 M $LiClO_4$, 10 mM LiI, and 1 mM $I_2$ at a scan rate of 50 mV/s, using a platinum sheet as the counter electrode, a SCE as the reference electrode, and the as-prepared CEs as the working electrode. Electrochemical impedance spectra (EIS) and Tafel polarization curves (TPCs) of various CEs were measured on a CHI-660D electrochemical workstation (CH Instruments, Inc., USA). The EIS were carried out at zero bias using symmetrical cells by applying an AC voltage with 10 mV amplitude in a frequency range from 0.05 Hz to 100 kHz. The resultant impedance spectra were fitted with ZsimpWin software. The Tafel Polarization Curves of the CEs were obtained using symmetrical cells at a scan rate of 10 mV/s. The electrolytes used in both EIS and TCP measurements were the same as those used in the DSSCs.

## Results and discussion

Fig. 1 is a schematic showing the electrochemical strategy for preparing the CoS nanosheets/graphene composite CEs. First, pristine GO layers were pre-prepared on the ITO substrate by spray-coating method. Then, the CoS nanosheet arrays were directly grown on the GO/ITO substrate by electrochemical deposition; meanwhile, the GO layers also were synchronously electrochemically reduced by removing oxygen-containing groups on the surface of GO layers, forming reduced GO (rGO) layers with highly electronic conductivity. The whole process is facile and fast. The as-prepared rGO-CoS nanosheet composite CEs are able to be directly assembled into DSSCs without needing additional post-treatments. The electrochemical strategy has come true, as corroborated by the results in Fig. 2 and Fig. 3.

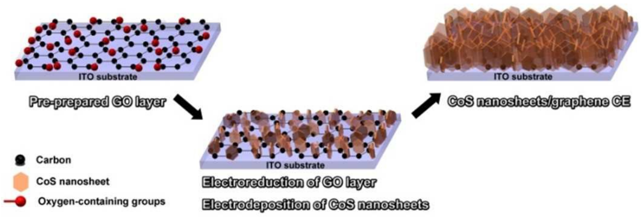

Fig. 1 Schematic of the electrochemical strategy for synchronously preparing composite CEs of CoS nanosheet arrays and reduced graphene oxide (rGO) layers.

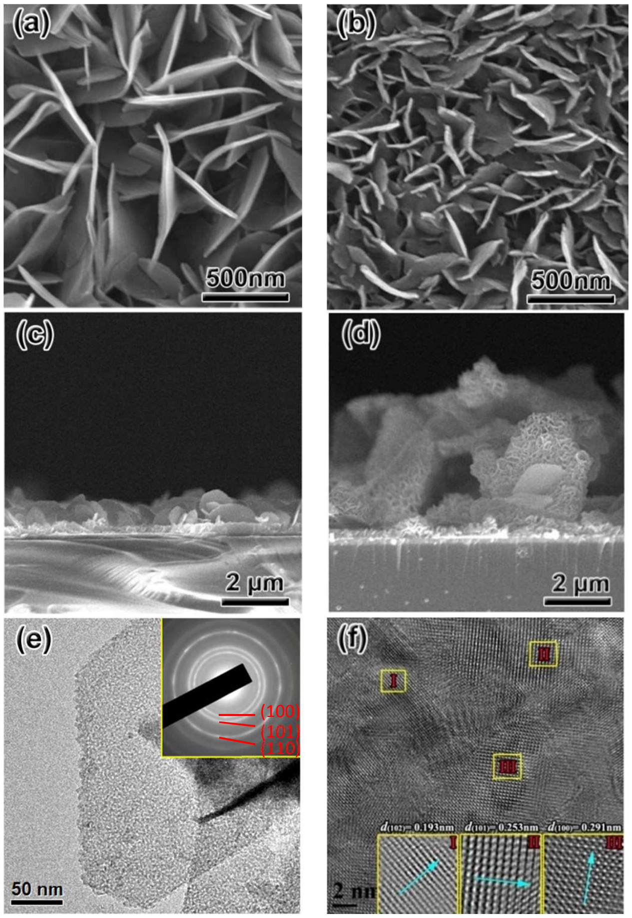

Fig. 2 SEM images of (a) pure CoS nanosheet CE and (b) rGO-CoS nanosheet composite CE, show the morphology evolution in the size and density. Cross section SEM images of (c) pure CoS nanosheet CE and (d) rGO-CoS nanosheet composite CE. (e) Low-magnification TEM image and SAED pattern (inset) of an individual CoS nanosheet from rGO-CoS composite CE, and continuous ring-like diffraction patterns show its polycrystalline nature. (f) Further high-resolution TEM image shows local morphology of the polycrystalline CoS nanosheet.

The morphology of the rGO-CoS nanosheet composite CEs is shown in Fig. 2b and exhibits 2D nanosheet arrays vertically grown on the rGO/ITO substrates, which is similar to the product directly electrodeposited on bare ITO substrate (Fig. 2a). However, after incorporating the GO layers, the former grew more densely, with smaller interspaces each other and show a distinct decrease in diameter from 0.6–0.8 μm to 0.3–0.4 μm. Besides, it is obvious from the cross section images (Fig. 2c-d) that CoS nanosheet arrays with about 1.4 μm in thickness were vertically electrodeposited on the ITO substrates for pure CoS CE, while hierarchical CoS nanosheet arrays with 5 μm in thickness were observed for rGO-CoS nanosheet composite CEs. The length of an individual CoS nanosheet is about 0.35 μm, consistent with the surface morphology observation in Fig. 2b. Noticeably, this unique structure is conducive to the transport of liquid electrolytes and exhibits larger active surface area for the reduction of $I_3^-$ ions. Generally, the binding effect existed between the negatively charged oxygen-containing groups on GO surface and the positively charged cations in solution. Therefore, a large number of active sites were provided by the GO layer for the crystal nucleation and growth of CoS nanosheets during the electro- deposition. As a result, smaller-sized, denser CoS nanosheet arrays were formed compared with the products without the incorporation of GO layers. The binding effect also was frequently applied to control the morphology and structure of the products hydrothermally grown on GO layers[31-32]. TEM image (Fig. 2c) of rGO-CoS composite film scraped from the substrate displays an individual 2D CoS nanosheet with the same morphology as SEM observation. Ring-like ED patterns (inset of Fig. 2c) of the nanosheet reveal its polycrystalline character. Further high-resolution TEM image of the nanosheets (Fig. 2d) shows that the zone I, II, and III correspond to the (102), (101), and (100) crystallographic planes of CoS, respectively, in good agreement with the polycrystalline conjecture.

Crystal phase of CoS nanosheets and rGO-CoS nanosheets also was confirmed by XRD measurements (Fig. 3a). Both the two CEs have the nearly same diffraction peaks located at 30°, 34°, and 35°, which can be readily indexed to the (100), (002), and (101) planes of the hexagonal phase CoS (JCPDS, PDF no. 75-0605). However, the diffraction peak of graphene at 26° is covered by the broad peak at around 23° for $SiO_2$ in the substrate due to the much smaller quantity of rGO layers compared to the substrate[30]. Therefore, raman spectroscopy was used to further corroborate the presence of rGO in the rGO-CoS composite CE, as shown in Fig. 3b. Two main characteristic peaks at 1356 $cm^{-1}$ and 1580 $cm^{-1}$ were observed in all samples, corresponding to the D-band and G-band of polycrystalline graphite[33], respectively. The G-band usually is assigned to the $E_{2g}$ phonons of C $sp^2$ atoms, while the D-band is attributed to the effect of particle size. From Fig. 3b, the D/G intensity ratios of GO and rGO are 0.786 and 0.84 respectively. This change is considered as the formation of more graphitic domains with smaller size upon electrochemical reduction[34–35]. Notably, the D/G ratio for the rGO-CoS composite CE is increased further to 1.03, which can be explained by the partial insertion of CoS nanosheets into the GO layers at the beginning of electrochemical process, thus resulting in more disordered carbon structure[31]. In addition, the small 2D peak at around 2750 $cm^{-1}$ was observed for both the rGO and rGO-CoS samples, further demonstrating the existence of rGO[36–37]. Fig. 3c presents the FTIR spectroscopy of the GO, rGO, and rGO-CoS composite CEs. Before reduction, the three bands of GO, evident at 1050 $cm^{-1}$, 1720 $cm^{-1}$, and 3430 $cm^{-1}$, are due, respectively, to the C–O (ν(epoxy or alkoxy)), the C=O in the carboxylic acid and carbonyl moieties (ν(carbonyl)), and the O–H stretching mode of intercalated water[34]. This result clearly reveals that exfoliated graphite has turned into graphene oxide via Hummer's method. However, in the case of pure rGO and rGO-CoS after electrochemical treatment, the peak at 3430 $cm^{-1}$ disappears, while other oxygen-containing stretches, such as C=O and C–O, also weaken. This result implies that high-purity rGO can be obtained using the electrochemical approach.

The electrocatalytic ability and conductivity of pure CoS, rGO-CoS, and Pt CEs were investigated by cyclic voltammetry (CV),

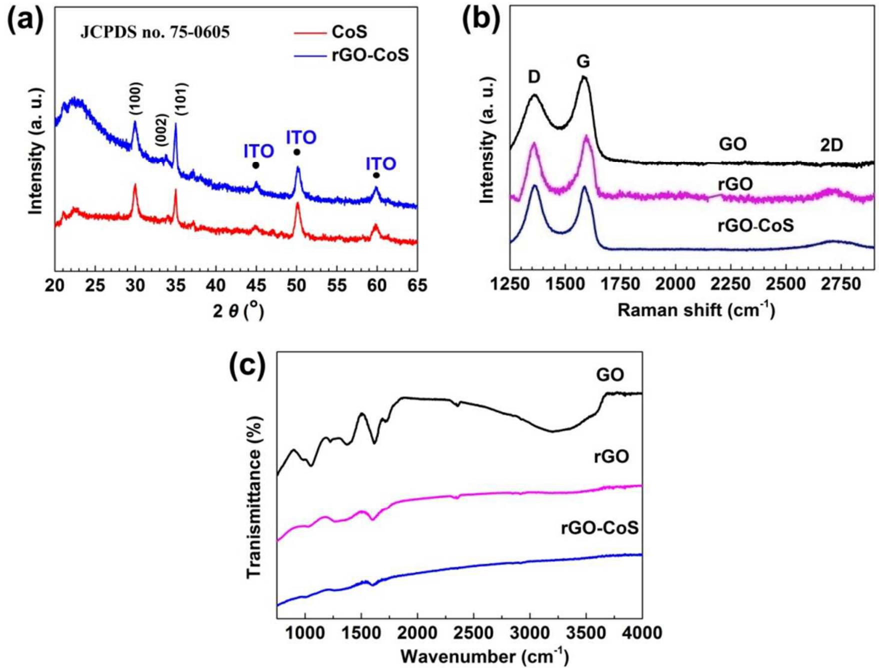

Fig. 3 (a) XRD patterns of CoS nanosheet and rGO-CoS nanosheet composite CEs. Both the two CEs have the nearly same diffraction peaks located at 30°, 34°, and 35°, which can be readily indexed to the (100), (002), and (101) planes of the hexagonal phase CoS. (b) Raman spectra of the GO layers, rGO layers, and rGO-CoS nanosheet composite CE. The increase in D/G intensity ratio and the emergence of small 2D peak at around 2750 $cm^{-1}$ corroborate the presence of rGO in the rGO-CoS composite CE. (c) FT-IR spectra of the GO layers, rGO layers, and rGO-CoS nanosheet composite CE, showing the successful transition from the GO to rGO by electrochemical reduction.

electrochemical impedance spectrum (EIS), and the Tafel polarization curve (TPC). From the CV results in Fig. 4a, two pairs of typical oxidation and reduction peaks clearly are observed for each CV curve. The left pair corresponds to the reaction of equation (1), and the right pair is attributed to the process of equation (2)[38]. Note that the left pair of peaks (Ox-1 and Red-1) is the main concerns of our analysis because the function of a DSSC CE is to catalyze the reduction of $I_3^-$ ions. Generally, the peak current density and the peak-to-peak separation ($E_{pp}$), which is associated with the reversibility of the redox reaction, are two important parameters for evaluating catalytic activities[39]. From Fig. 4a, the rGO-CoS composite CE has the highest peak current density, implying that the electrocatalytic ability of rGO-CoS CE toward $I^-/I_3^-$ is superior to that of pure CoS and even better than that of Pt. In addition, its $E_{pp}$ of 570 mV is lower than 680 mV of CoS. Thus, we confirmed that the rGO-CoS composite CE prepared by the one-step electrochemical method is a remarkable electrochemical catalyst.

$$I_3^- + 2e^- \leftrightarrow 3I^- \qquad (1)$$

$$3I_2 + 2e^- \leftrightarrow 2I_3^- \qquad (2)$$

EIS represents the intrinsic interfacial charge transfer and charge transport kinetics at the electrode/electrolyte interface[40]. It has been tested using symmetric cells fabricated with two identical electrodes. Fig. 4b demonstrates the Nyquist plots of pure CoS, rGO-CoS, and Pt CEs, respectively. The inset shows the equivalent circuit model used for DSSCs. As displayed in Fig. 4b, the high-frequency intercept on the real axis determines the serial resistance ($R_s$), while two semicircles observed for each curve in the high-frequency (left) and low-frequency (right) regions are assigned, respectively, to the charge-transfer resistance ($R_{ct}$) at the electrode/electrolyte interface, and the ionic diffusion impedance ($Z_N$) of the $I^-/I_3^-$ redox couple in the electrolyte[41]. Table 1 lists the fit data for $R_s$ and $R_{ct}$. Obviously, the $R_s$ value decreases for the rGO-CoS composite CE compared with pure CoS CE, revealing that the incorporation of rGO layers is beneficial for improving the conductivity of rGO-CoS. Moreover, the rGO-CoS CE has the smallest $R_{ct}$ of 2.1 $\Omega$ $cm^2$. The value is slightly lower than that of Pt CE, and only one third of 7.1 $\Omega$ $cm^2$ of pure CoS CE. This result suggests that the incorporation of rGO layers can markedly decrease the internal resistance and thus accelerate the reduction process of $I_3^-$ to $I^-$ at the electrode/electrolyte interface. TPC also was conducted on the same symmetric cells used for EIS measurements to further elucidate the

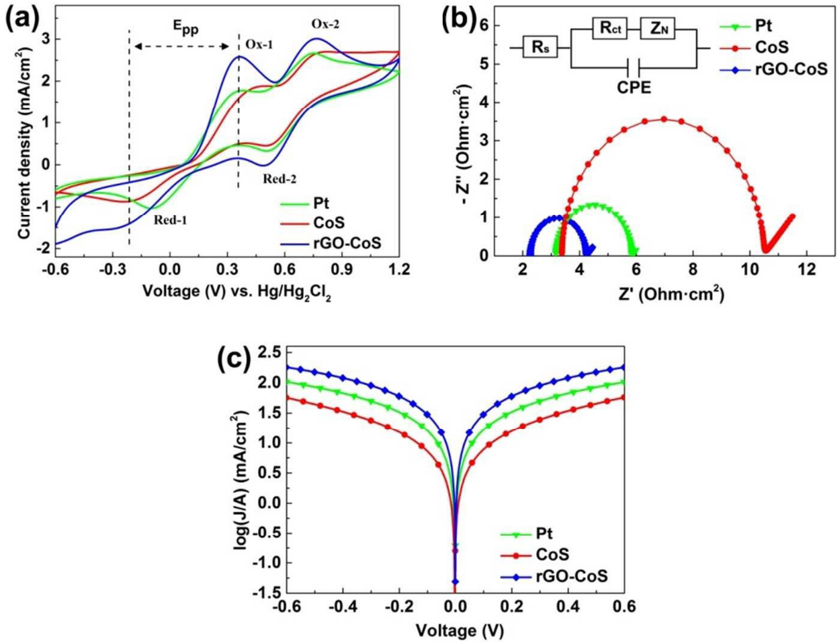

Fig. 4 (a) CV curves of iodide/triiodide redox species for Pt CE, pure CoS nanosheet CE and rGO-CoS nanosheet composite CE, obtained in ACN solution containing 10.0 mM LiI, 1.0 mM $I_2$, and 0.1 M $LiClO_4$, at a scan rate of 50 mV/s. (b) Nyquist plots and (c) Tafel polarization curves of Pt, pure CoS nanosheet and rGO-CoS nanosheet composite CEs, obtained with two identical electrodes in the same electrolyte as that used in DSSCs at a scan rate of 10 mV/s. Inset in b gives the equivalent circuit used in DSSCs.

catalytic activity for the $I_3^-$ reduction of Pt, CoS, and rGO-CoS CEs. From Fig. 4c, the rGO-CoS composite CE shows the largest slope of the anodic or cathodic branches around the Tafel zone compared with the Pt and pure CoS CEs, suggesting a higher exchange current density ($J_o$) on the electrode surfaces[42]. Since $J_o$ also is related to the charge-transfer resistance ($R_{ct}$), it also can be calculated by equation (3) ,

$$J_o = \frac{RT}{nFR_{ct}} \qquad (3)$$

Where $R$ is the gas constant, $F$ is Faraday's constant, $T$ is the absolute temperature, and $n$ is the number of electrons involved with the reduction of $I_3^-$. Accordingly, the calculated $J_o$ follows the order of rGO-CoS > Pt > CoS, in good agreement with the tendency of the peak current density observed in the CV curves and EIS results.

Photocurrent density-voltage (*J-V*) curves of the DSSCs with pure CoS, rGO-CoS, and commercial Pt CEs were obtained under a light intensity of 100 mW/cm². A typical schematic configuration of the DSSC is illustrated in Fig. 5a and the *J-V* curves obtained are shown in Fig. 5b. The inset compares the optical photographs of the rGO-CoS composite CE and pure CoS CE. The photovoltaic parameters are summarized in Table 1. The DSSC with pure CoS CE yielded a PCE of 6.26%, comparable to that obtained in previous research[16]. Its photocurrent density ($J_{sc}$) is only 13.82 mA/cm², which is the lowest among the three DSSCs; on the contrary, the $J_{sc}$ of the DSSC with rGO-CoS composite CE is the highest (17.03 mA/cm²), around 23% increase compared with that of pure CoS-based DSSC. Therefore, the DSSC with the rGO-CoS composite CE achieved an enhanced PCE of 8.34% that is greatly increased by 33% compared with 6.26% of the CoS CE-based DSSC. Noticeably, the enhanced PCE is even superior to 7.5% of Pt CE-based DSSC. This demonstrated the feasibility of using the rGO-CoS CE to supersede the costly traditional Pt CE.

**Table 1** Photovoltaic parameters of the DSSCs assembled with Pt CE, CoS nanosheet CE, and rGO-CoS nanosheet composite CE measured under a light intensity of 100 mW/cm².

| CEs | $V_{oc}$ (V) | $J_{sc}$ (mA /cm²) | FF | PCE (%) | $R_s$ (Ω cm²) | $R_{ct}$ (Ω cm²) |
|---|---|---|---|---|---|---|
| Pt | 0.76 | 16.83 | 0.59 | 7.50 | 3.2 | 2.7 |
| CoS | 0.76 | 13.82 | 0.59 | 6.27 | 3.4 | 7.1 |
| rGO-CoS | 0.77 | 17.02 | 0.63 | 8.34 | 2.2 | 2.1 |

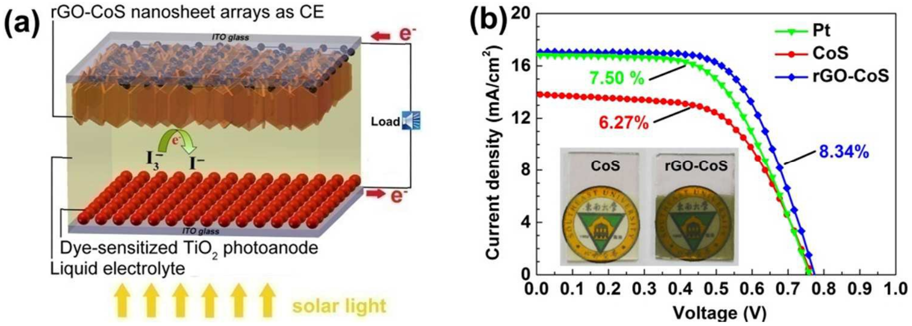

Fig. 5 (a) Schematic diagram of a DSSC assembled with the rGO-CoS composite CE. (b) Photocurrent density−voltage (*J*-*V*) curves of DSSCs constructed using Pt CE, CoS nanosheet CE and the rGO-CoS composite CE under a simulated solar illumination with a light intensity of 100 mW/cm$^2$ (AM 1.5). Inset in (b) compares the optical photos of pure CoS CE and rGO-CoS composite CE.

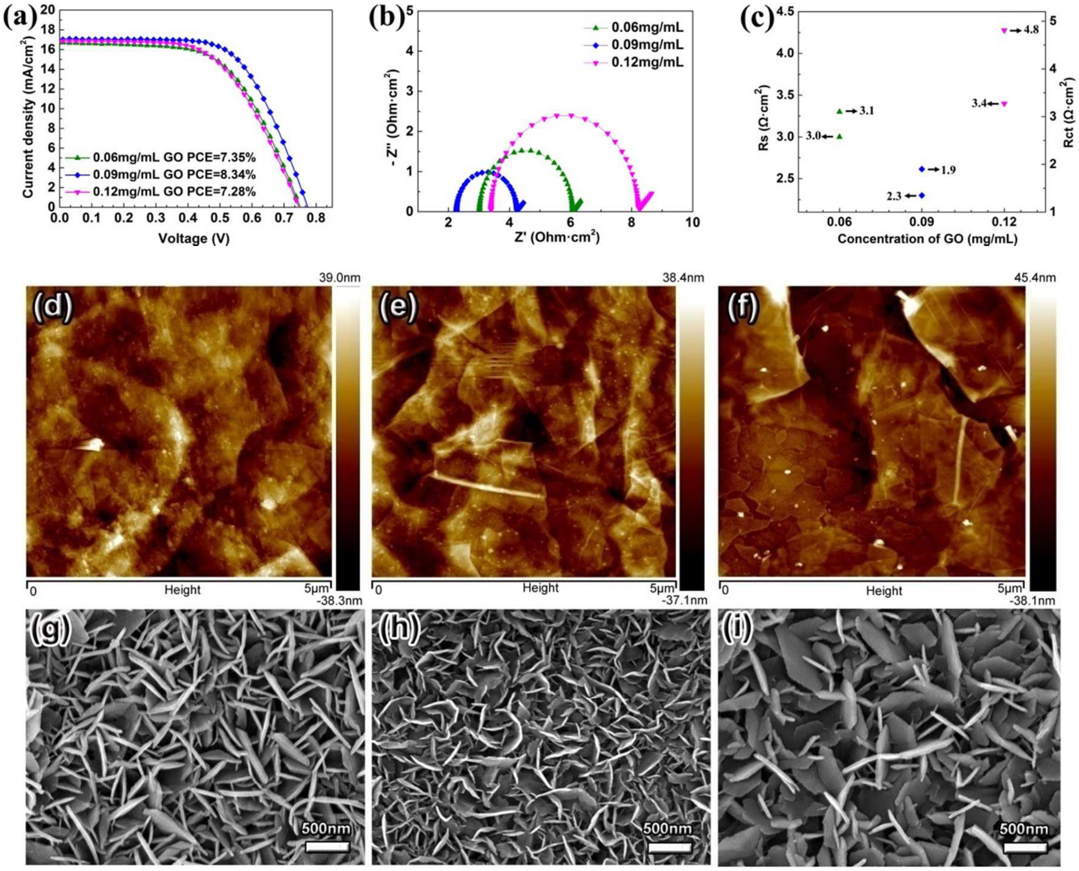

Fig. 6 (a) The photocurrent density−voltage (*J*-*V*) curves of DSSCs assembled using the rGO-CoS composite CEs fabricated with GO concentrations of 0.06 mg/mL, 0.09 mg/mL, and 0.12 mg/mL, respectively, under a simulated solar illumination with a light intensity of 100 mW/cm$^2$ (AM 1.5). (b) The EIS spectra of composite CEs were tested at a scan rate of 10 mV/s with two identical electrodes in the same electrolyte as that used in DSSCs. (c) The serial resistance ($R_s$) and charge-transfer resistance ($R_{ct}$) of composite CEs fabricated with different concentrations of GO. (d−f) AFM images of GO layers fabricated with GO concentrations of 0.06 mg/mL, 0.09 mg/mL, and 0.12 mg/mL, respectively, showing the effect of GO concentration on morphology of GO layers. (g–i) SEM images of the as-prepared rGO-CoS nanosheet arrays directly electrodeposited on the GO layers corresponding to (d−f) counterparts, respectively.

**Table 2** Comparison of graphene-CoS composite CEs fabricated by different methods.

| Synthesis methods | Structure | Heating | Total time | PCE(%) | Ref. |
|---|---|---|---|---|---|
| CVD/dip-coating/Annealing | Graphene-CoS nanoparticle | 1000 ℃ | 15h | 5.04 | 24 |
| Hydrothermal/Doctor-blade | Graphene-CoS nanoparticle | 160-180 ℃ | 12–18h | 6.55/7.08 | 25, 43 |
| Electrophoretic/Annealing/Solvo-thermal | Graphene-CoS nanoparticle | 400 ℃ | 30h | 5.54 | 27 |
| Hydrothermal/Spray-coating/Annealing | Graphene-CoS nanoparticle | 200 ℃ | 15h | 7.05 | 42 |
| Spray-coating/Electrochemical | Graphene-CoS nanosheet | 40 ℃ | 0.5h | 8.34 | Our work |

The outstanding PCE breakthrough is indubitably attributed to the incorporation of conducting rGO layers and the GO layers-induced growth of CoS nanosheet arrays. As displayed in SEM observations, the GO layers-induced growth of CoS exhibits hierarchical structure with smaller nanosheets and denser arrays. This unique structure benefits the transport of liquid electrolytes and provides a larger active surface area on the electrode for the reduction reaction of triiodide ions. Particularly, it is favorable to increase the exchange current density, thus boosting the $J_{sc}$ value[24,42]. Moreover, the incorporation of conductive rGO layers and the optimized CoS nanostructure also greatly decrease the internal resistance of rGO-CoS composite CE ($R_s$ and $R_{ct}$), as corroborated by the EIS measurements (Table 3). The lowered $R_s$ and $R_{ct}$ of rGO-CoS nanosheets CE could promote the collection of electrons from the external circuit and enhance the charge transfer from the CE to triiodide ions, consequently attributing to the enhancement of FF value[42]. In view of these two aspects, the DSSC device based on rGO-CoS nanosheets CE achieves superior photoelectric performance to that based on pure CoS CE.

Since introducing rGO layers can greatly improve the properties of CEs and thus enhance the PCE of DSSCs, the GO loading content on substrates should be a paramount issue in deciding cell performance. Fig. 6a demonstrates the compared current-voltage (*J-V*) characteristics and EIS parameters based on rGO-CoS CEs fabricated by spray-coating GO solutions with different concentrations. All the DSSCs with rGO-CoS composite CEs show higher PCEs compared with the DSSC with pure CoS CE in Fig. 5b. The PCE increased from 7.35% to 8.34% with increasing GO concentration from 0.06 mg/mL to 0.09 mg/mL, and then declines to 7.28% corresponding to concentration of 0.12 mg/mL. The changes in PCE can be explained by the EIS measurements in Fig. 6b and c, which reveal that the $R_s$ and $R_{ct}$ of rGO-CoS CEs follow the order of 0.12 mg/mL > 0.06 mg/mL > 0.09 mg/mL, *i.e.*, totally consistent with the change tendency of PCE. Further AFM investigation (Fig. 6 d–f) shows that GO concentration of 0.09 mg/mL exhibit a relatively flat morphology, whereas the high-concentration GO solution resulted in wrinkles and stacking, which would increase the serial resistance, as reflected by the EIS results. In turn, the wrinkles and stacking of GO layers also greatly affectsthe morphology of CoS nanosheet arrays, including their density and size (Fig. 6 g–i). Obviously, the CoS nanosheet arrays grown on GO layers with a concentration of 0.09 mg/mL exhibits a higher density and smaller size, which would provide a larger surface area for yielding a higher exchange current. The extensive investigation proves that GO layers exert a correlative effect on the resultant DSSC performance.

Our electrochemical strategy for preparing the rGO-CoS CEs exhibits attractive superiorities compared with other approaches including conventional hydrothermal or CVD methods, as summarized in Table 2. The strategy allows the deposition of CoS nanosheets and the reduction of GO at low temperature, and requires relatively inexpensive equipments. The whole process of fabricating the CEs is facile without additional post-treatments including the doctor-blade or spray-coating procedures[25,42–43]. Importantly, it provides a ultrafast route to prepare the rGO-CoS CE only in half an hour, which is several tens of times shorter than the average time (~15 h) using other approaches (Table 2). Due to the superior electrocatalytic activity, the composite films directly prepared on substrates produced a high PCE of 8.34%, indicating

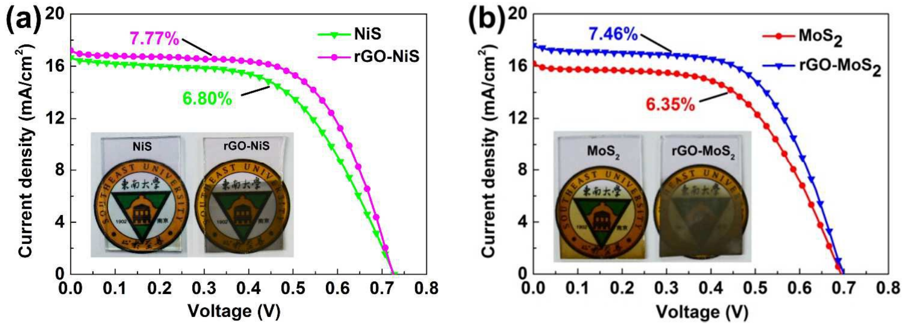

Fig. 7 Photocurrent density−voltage (*J-V*) curves of the DSSCs assembled using (a) rGO-NiS composite CE and pure NiS CE, (b) rGO-$MoS_2$ composite CE and $MoS_2$ CE under a simulated solar illumination with a light intensity of 100 mW/cm$^2$ (AM 1.5). The insets show their optical photos, respectively.

**Table 3** Comparison of photovoltaic parameters of the DSSCs assembled with rGO-NiS composite CEs and rGO-$MoS_2$ composite CEs fabricated by different methods measured under a light intensity of 100 mW/$cm^2$.

| CE | Synthesis methods | $V_{oc}$ (V) | $J_{sc}$ (mA /$cm^2$) | FF | PCE (%) | Ref. |
|---|---|---|---|---|---|---|
| Graphene-NiS | Spray-coating/Electrochemical | 0.73 | 17.00 | 0.63 | 7.77 | Our work |
| Graphene-NiS | CVD/Dip-coating/Annealing | 0.72 | 10.31 | 0.7 | 5.25 | 24 |
| Graphene-$MoS_2$ | Spray-coating/Electrochemical | 0.70 | 17.41 | 0.61 | 7.46 | Our work |
| Graphene-$MoS_2$ | Hydrothermal/Electrophoretic | 0.77 | 12.79 | 0.59 | 5.81 | 45 |
| Graphene-$MoS_2$ | Thermal pyrolysis/Reduction/Drop-casting | 0.73 | 12.51 | 0.66 | 6.04 | 46 |

the unparalleled advantages of our electrochemical strategy in preparing the composite CEs. Furthermore, the electrochemical strategy also exhibits its universality in fabricating graphene-enhanced chalcogenide functional composite films. Here, we, for the first time, used the strategy to prepare rGO-$MoS_2$ and rGO-NiS composite CEs[12,44] that also exhibited enhanced performances in DSSCs compared with the previous works[24,45-46], as shown in Fig. 7 and Table 3. Similarly, the fabrication process of both the two composite CEs also was ultrafast. Based on the above results, we believe that electrochemical strategy could be a universal method for fabrication of graphene-enhanced chalcogenide functional composite films.

## Conclusions

In conclusion, we presented a facile, low temperature, and ultrafast electrochemical strategy to fabricate the rGO-CoS composite CEs that are low-cost and high-efficiency and can supersede costly traditional Pt CE in DSSCs. In this strategy, electroreduction of original GO layers and electrodeposition of CoS nanosheet arrays was synchronous. It's demonstrated that the incorporation of rGO layers could greatly decrease the charge-transfer resistance and improve the electrocatalytic ability. Furthermore, the GO layers-induced growth of CoS nanosheet arrays with higher density and larger surface area can provide larger surface area for yielding higher exchange current. Thus, the DSSC based on the optimized rGO-CoS composite CEs showed marked enhancement in PCE compared with the previously reported works involved with other fabrication approaches. Further experiments also proved that our electrochemical strategy has potential for further exploiting other graphene-enhanced chalcogenide functional composite films with applications in electronic and optoelectronic devices.

## Acknowledgements

This work was supported by the National Basic Research Program of China (973 Program, Grant No. 2015CB352106), the National Natural Science Foundation of China (NSFC, Grant Nos. 61574034, 51372039, and 51202028), the Jiangsu Province Science and Technology Support Program (Grant No. BK20141118), the Fundamental Research Funds for the Central Universities (Grant Nos. 2242013R30004), China Postdoctoral Science Foundation Funded Project (Grant Nos. 2014M550259 and 2015T80480). The work at Brookhaven National Lab is supported by U.S. DOE-BES under Contract number DE-AC02-98CH10886.

## Reference

1 W. Q. Wu, H. L. Feng, H. S. Rao, Y. F. Xu, D. B. Kuang and C. Y. Su, *Nat. Commun.*, **2014**, 5, 396
2 S. N. Yun, A. Hagfeldt and T. L. Ma, *Adv. Mater.*, **2014**, 26, 6210–6237.
3 F. Xu, J. Chen, X. Wu, Y. Zhang, Y. X. Wang, J. Sun, H. C. Bi, W. Lei, Y. R. Ni and L. T. Sun, *J. Phys. Chem. C*, **2013**, 117, 8619–8627.
4 G. Calogero, P. Calandra, A. Irrera, A. Sinopoli, I. Citro and G. D. Marco, *Energy Environ. Sci.*, **2011**, 4, 1838–1844
5 V. D. Dao, S. H. Kim, H. S. Choi, J. H. Kim, H. O. Park and J. K. Lee, *J. Phys. Chem. C*, **2011**, 115, 25529–25534
6 J. W. Wan, G. J. Fang, H. J. Yin, X. F. Liu, D. Liu, M. T. Zhao, W. J. Ke, H. Tao and Z. Y. Tang, *Adv. Mater*., **2014**, 26, 8101–8106.
7 Z. Y. Tang, J. H. Wu, M. Zheng, Q. W. Tang, Q. Liu, J. M. Lin and J. L. Wang, *RSC Adv.*, **2012**, 2, 4062–4064.
8 M. X. Wu, X. Lin, T. H. Wang, J. S. Qiu and T. L. Ma, *Energy Environ. Sci.*, **2011**, 4, 2308–2315.
9 Y. H. Xue, J. Liu, H. Chen, R. G. Wang, D. Q. Li, J. Qu and L. M. Dai, *Angew. Chem. Int. Ed.*, **2012**, 51, 12124–12127.
10 S. J. Peng, P. N. Zhu, Y. Z. Wu, S. G. Mhaisalkara and S. Ramakrishna, *RSC Adv.*, **2012**, 2, 652–657.
11 J. Kwon, V. Ganapathy, Y. H. Kim, K. D. Song, H. G. Park, Y. Jun, P. J. Yoo and J. H. Park, *Nanoscale*, **2013**, 5, 7838–7843.
12 H. C. Sun, D. Qin, S. Q. Huang, X. Z. Guo, D. M. Li, Y. H. Luo and Q. B. Meng, *Energy Environ. Sci.*, **2011**, 4, 2630–2637.
13 Z. Y. Zhang, S. P. Pang, H. X. Xu, Z. Z. Yang, X. Y. Zhang, Z. H. Liu, X. G. Wang, X. H. Zhou, S. M. Dong, X. Chen, L. Gu and G. L. Cui, *RSC Adv.*, **2013**, 3, 16528–16533.
14 M. Al-Mamun, H. Zhang, P. Liu, Y. Wang, J. Caoac and H. J. Zhao, *RSC Adv.*, **2014**, 4, 21277-21283.
15 J. Y. Lin, J. H. Liao and S. W. Chou, *Electrochim. Acta*, **2011**, 56, 8818–8826.
16 C. W. Kung, H. W. Chen, C. Y. Lin, K. C. Huang, R. Vittal and K. C. Ho, *ACS Nano*, **2012**, 6, 7016–7025.
17 M. K. Wang, A. M. Anghel, B. Marsan, N. C. Ha, N. Pootrakulchote, S. M. Zakeeruddin and M. Gratzel, *J. Am. Chem. Soc.*, **2009**, 131, 15976–15977.
18 W. X. Guo, C. Chen, M. D. Ye, M. Q. Lv and C. J. Lin, *Nanoscale*, **2014**, 6, 3656–3663.
19 M. I. Katsnelson, *Mater. Today*, **2007**, 10, 20–27.
20 M. Y. Yen, C. K. Hsieh, C. C. Teng, M. C Hsiao, P. Liu, C. M. Ma, M. C. Tsai, C. H. Tsai, Y. R. Lin and T. Y. Chou, *RSC Adv.*, **2012**, 2, 2725-2728.
21 Y. Peng, J. Zhong, K. Wang, B. F. Xue and Y. B. Cheng, *Nano Energy*, **2013**, 2, 235–240.
22 H. Wang and Y. H. Hu, *Energy Environ. Sci.*, **2012**, 5, 8182–8188.
23 S. Das, P. Sudhagar, S. Nagarajan, E. Ito, S. Y. Lee, Y. S. Kang and W. B. Choiet, *Carbon*, **2012**, 50, 4815–4821.
24 H. Bi, W. Zhao, S. R. Sun, H. L. Cui, T. Q. Lin, F. Q. Huang, X. M. Xie and M. H. Jiang, *Carbon*, **2013**, 61, 116–123.
25 X. L. Duan, Z. Y. Gao, J. L. Chang, D. P. Wu, P. F. Ma, J. J. He, F. Xu, S. Y. Gao and K. Jiang, *Electrochim. Acta*, **2013**, 114, 173–179.
26 H. W. Hu, J. N. Ding, J. F. Qian, Y. Li, L. Bai and N. Y. Yuan, *Mater. Lett.*, **2014**, 114, 7–10.
27 X. H. Miao, K. Pan, G. F. Wang, Y. P. Liao, L. Wang, W. Zhou, B. J. Jiang, Q. J. Pan and G. H. Tian, *Chem. Eur. J.*, **2014**, 20, 474–482.
28 H. C. Bi, K. B. Yin, X. Xie, Y. L. Zhou, N. Wan, F. Xu, F. Banhart, L. T. Sun and R. S. Ruoff, *Adv. Mater.*, **2012**, 24, 5124–5129.
29 W. S. Hummers and R. E. Offeman, *J. Am. Chem. Soc.*, **1958**, 80, 1339.

30 Y. G. Zhou, J. J. Chen, F. B. Wang, Z. H. Sheng and X. H. Xia, *Chem. Commun.*, **2010**, 46, 5951–5953.
31 Y. Gu, Y. Xu and Y. Wang, *ACS Appl. Mater. Interf.*, **2013**, 5, 801–806.
32 Y. Q. Zou and Y. Wang, *Nanoscale*, **2011**, 3, 2615–2620.
33 F. Tuinstra and J. L. Koenig, *J. Chem. Phys.*, **1970**, 53, 1126–1130.
34 H. L. Guo, X. F. Wang, Q. Y. Qian, F. B. Wang and X. H. Xia, *ACS Nano*, **2009**, 3, 2653–2659.
35 S. Stankovich, D. A. Dikin, R. D. Piner, K. A. Kohlhaas, A. Kleinhammes, Y. Y. Jia, Y. Wu, S. T. Nguyen and R. S. Ruoff, *Carbon*, **2007**, 4, 1558–1565.
36 A. C. Ferrari, *Solid State Commun.*, **2007**, 143, 47–57.
37 A. C. Ferrari, J. C. Meyer, V. Scardaci, C. Casiraghi, M. Lazzeri, F. Mauri, S. Piscanec, D. Jiang, K. S. Novoselov, S. Roth and A. K. Geim, *Phys. Rev. Lett.*, **2006**, 97, 187401.
38 F. Gong, H. Wang, X. Xu, G. Zhou and Z. S. Wang, *J. Am. Chem. Soc.*, **2012**, 134, 10953–10958.
39 J. D. Roy-Mayhew, D. J. Bozym, C. Punckt and I. A. Aksay, *ACS Nano*, **2010**, 4, 6203–6211.
40 X. J. Zheng, J. Deng, N. Wang, D. H. Deng, W. H. Zhang, X. H. Bao and C. Li, *Angew. Chem. Int. Ed.*, **2014**, 53, 7023–7027.
41 J. H. Guo, Y. T. Shi, Y. T. Chu and T. L. Ma, *Chem. Commun.*, **2013**, 49, 10157–10159.
42 E. B. Bi, H. Chen, X. D. Yang, W. Q. Peng, M. Gratzel and L. Y. Han, *Energy Environ. Sci.*, **2014**, 7, 2637–2641.
43 G. Q. Wang, J. Zhang, S. Kuang, S. M. Liu and S. P. Zhuo, *J. Power Sources*, **2014**, 269, 473–478.
44 S. Chen, J. J. Duan, Y. H. Tang, B. Jin and S. Z. Qiao, *Nano Energy*, **2015**, 11, 11–18.
45 J. Y. Lin, C. Y. Chan and S. W. Chou, *Chem. Commun.*, **2013**, 49, 1440–1442.
46 C. J. Liu, S. Y. Tai, S. W. Chou, Y. C. Yu, K. D. Chang, S. Wang, F. S. S. Chien, J. Y. Lin and T. W. Lin, *J. Mater. Chem.*, **2012**, 22, 21057–21064.